


 Cite this: *Chem. Commun.*, 2022, 58, 11575

 Received 28th July 2022,  
 Accepted 21st September 2022

DOI: 10.1039/d2cc04126j

[rsc.li/chemcomm](http://rsc.li/chemcomm)

**Chiral plasmonic nanocrystals with varied symmetries were synthesized by L-glutathione-guided overgrowth from Au tetrahedra, nanoplates, and octahedra, highlighting the importance of chiral molecule adsorption at transient kink sites. Large *g*-factors are possible and depend on symmetry. Simulations of their chiroptical properties from tomographically obtained nanocrystal models further verify their chirality.**

Chiral plasmonic nanocrystals are of interest for their enantiospecific interactions with light,<sup>1</sup> having been achieved synthetically by colloidal and lithographic methods.<sup>1–6</sup> One method toward chiral plasmonic nanocrystals exploits enantioselective adsorption of chiral molecules on seed surfaces, where transfer of molecular chirality to metal nanocrystal systems has been achieved during seeded overgrowth.<sup>7,8</sup> Lee *et al.* proposed that such adsorption occurs predominantly on intrinsically chiral surfaces with high Miller indices.<sup>1</sup> That is, transient kink sites formed at the intersection of thermodynamically favorable nanocrystal facets, *e.g.*, the {111}, {100}, and {110} facets of face-centered cubic metals, facilitate enantioselective adsorption of chiral molecules.<sup>1,9</sup> This handed interaction, in turn, leads to chiral nanocrystal shapes during overgrowth through preferential expression of one (*R/S*)-handed chiral surface over the other.

This approach has yielded chiral Au helicoids seeded from Au cubes, octahedra, and rhombic dodecahedra.<sup>1,10</sup> The enantiomeric form of the final helicoids has been controlled through the selection of the chiral molecule (*e.g.*, *L*- versus *D*-cysteine).<sup>1</sup> The resulting helicoid nanocrystals exhibit strong chiroptical behavior, most notably 432 helicoid III which is formed from a single-step chiral overgrowth of octahedral Au

## Seed-directed synthesis of chiroptically active Au nanocrystals of varied symmetries†

 Jack S. Googasian,<sup>a</sup> George R. Lewis,<sup>b</sup> Zachary J. Woessner,<sup>a</sup> Emilie Ringe<sup>ib</sup> \*<sup>b</sup> and Sara E. Skrabalak<sup>ib</sup> \*<sup>a</sup>

seeds and boasts a *g*-factor of approximately 0.2, defined here as:

$$\frac{\text{CD}}{\text{extinction}} \propto \frac{2(A_L - A_R)}{(A_L + A_R)} = g\text{-factor} \quad (1)$$

where  $A_L$  and  $A_R$  are the absorbances of left and right circularly polarized light, respectively, CD is the circular dichroism, and *g*-factor is a dimensionless dissymmetry factor that is used for chiroptical property comparisons between systems. For example, chiral molecules, lithographically-obtained arrays, and templated assembly systems can be directly compared with reported *g*-factors of approximately  $5 \times 10^{-3}$ ,  $7 \times 10^{-1}$ , and  $3 \times 10^{-2}$ , respectively.<sup>1,11,12</sup> Bottom-up synthesis of chiral nanocrystals presents an exciting frontier to obtain scalable chiroptical activity; however the molecular-templated, face-directed overgrowth employed in previous works is currently limited to nanocrystal seeds with octahedral ( $O_h$ ) symmetry.

Here, we show this approach can be applied to other nanocrystal seeds, including those with dihedral ( $D_{3h}$ ) and tetrahedral ( $T_d$ ) symmetries. We note that the use of point group notation for different nanocrystal types reflects idealized structures without consideration of slight imperfections. Considering the formation of 432 helicoid III, overgrowth from Au octahedra was mediated with L-glutathione (L-GSH) as a chiral additive, moving from a system with  $O_h$  symmetry to one with octahedral rotational ( $O$ ) symmetry and the loss of mirror symmetry.<sup>13</sup> Note that we are specifically referring to the overall nanocrystal symmetry and not the FCC crystal structure. For comparison, triangular Au plates and Au tetrahedra with  $D_{3h}$  and  $T_d$  symmetries, respectively, were selected for L-GSH-mediated overgrowth of additional Au. Notably, both the triangular Au plates and tetrahedra are terminated with {111} facets, just like the octahedral Au seeds used in the 432 helicoid III system, allowing for a direct comparison of symmetry effects during L-GSH-mediated overgrowth.

Considering the dihedral symmetry case, triangular Au plates (edge length:  $38 \pm 3$  nm, Fig. 1a) were synthesized through reduction of HAuCl<sub>4</sub> with L-ascorbic acid (L-AA) in the

<sup>a</sup> Department of Chemistry, Indiana University – Bloomington, 800 E. Kirkwood Ave., Bloomington, IN 47405, USA. E-mail: sskrabal@indiana.edu

<sup>b</sup> Department of Materials Science & Metallurgy, University of Cambridge, 27 Charles Babbage Road, Cambridge, CB3 0FS, UK. E-mail: er407@cam.ac.uk

† Electronic supplementary information (ESI) available. See DOI: <https://doi.org/10.1039/d2cc04126j>



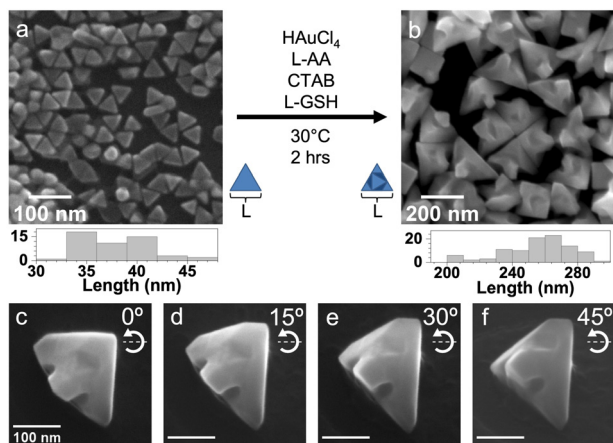


Fig. 1 SEM images of (a) triangular Au plate seeds and (b) overgrowth product with histograms of nanocrystal edge lengths below. (c–f) SEM images of a single Au nanocrystal after overgrowth at tilts denoted in upper right.

presence of NaI and cetyltrimethylammonium chloride (CTAC).<sup>14</sup> Then, these triangular Au plates were used as seeds to which additional Au was deposited from the reduction of  $\text{HAuCl}_4$  in the presence of L-GSH and cetyltrimethylammonium bromide (CTAB). Full experimental details can be found in the ESI.† The resulting Au nanocrystals are larger than the seeds, with an average edge length of  $255 \pm 21$  nm (Fig. 1b). There is transfer of dihedral 3-fold rotational symmetry from seed to product as well; however, Au protrudes from the face-centers of the triangular Au plates. Additionally, scanning electron microscopy (SEM) images of the same nanocrystal at different angles reveal concavities or material gaps within the protrusions (Fig. 1c–f).

Notably, when the same overgrowth procedure is conducted without L-GSH, larger Au nanocrystals are produced, again with protrusions from the face-centers of the triangular Au plates. However, concavities or gap indentations are not evident (Fig. S1, ESI†). This observation indicates that the chiral additive is required to achieve the 3-fold concave gap features. As will be discussed shortly, the Au nanocrystals with the 3-fold concave gaps display a chiroptical response while those without do not. However, notable chiral features are not immediately evident, particularly when comparing them to the 432 helicoid III obtained from overgrowth on Au octahedra (Fig. S2, ESI†), reproduced from Lee *et al.*<sup>1</sup> We attribute these observations to subtle differences in the surface terminations of Au octahedra and triangular Au plates. Both are encased by  $\{111\}$  facets, but Au octahedra are single-crystalline whereas triangular Au plates contain stacking faults enclosed by either  $\{110\}$  or  $\{1\bar{1}0\}$  edges.<sup>15</sup> The latter likely does not present all the necessary intersecting planes to facilitate expression of intrinsically chiral kink sites during overgrowth until after substantial metal has deposited.

Considering the  $T_d$  symmetry case, Au tetrahedra (edge length:  $80 \pm 3$  nm, Fig. 2a) were synthesized by reducing  $\text{HAuCl}_4$  with L-AA in the presence of CTAC, CTAB, and preformed Au spheres.<sup>16</sup> These tetrahedra were used as seeds onto which Au was deposited by reducing  $\text{HAuCl}_4$  with L-AA in the presence of

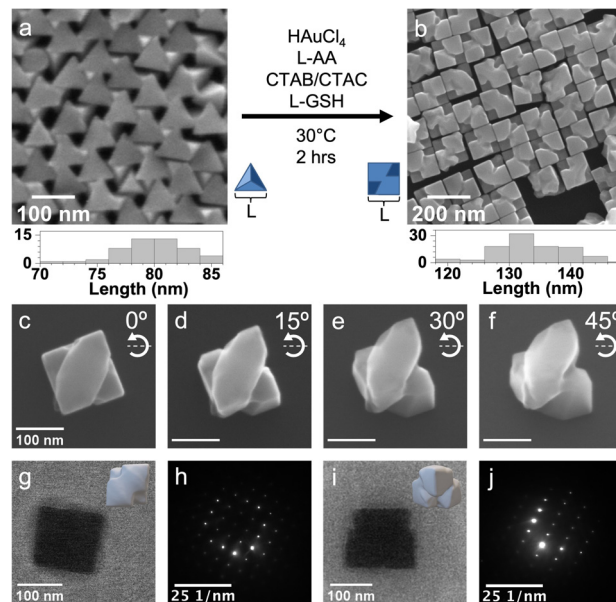
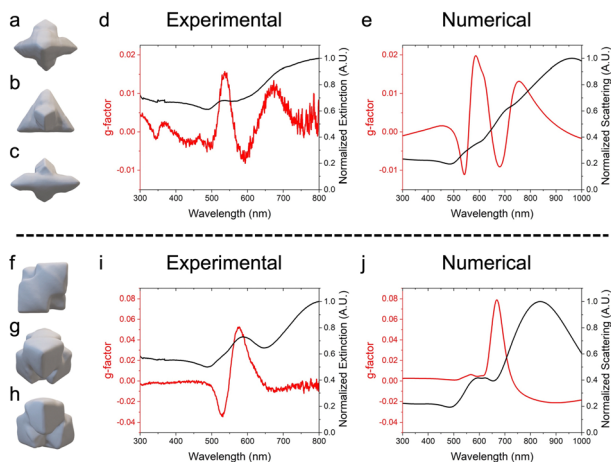


Fig. 2 SEM images of (a) tetrahedral Au seeds and (b) overgrowth product with histograms of nanocrystal edge lengths below. (c–f) SEM images of a single Au nanocrystal after overgrowth at tilts denoted in upper right. TEM images of overgrowth product along the (g) [100] and (i) [110] directions with representative tomographic reconstruction oriented to align with projection. Corresponding electron diffraction data in the (h) [100] and (j) [110] directions.

CTAC, CTAB, and L-GSH. The surfactant system was modified from CTAB to a mixture of CTAB and CTAC in a ratio consistent with the tetrahedral Au seed synthesis to increase nanocrystal growth rate and promote chiral expression,<sup>17,18</sup> otherwise, nearly cubic Au nanocrystals with a weak  $g$ -factor response were produced with CTAB only (Fig. S3, ESI†). Note that the synthetic conditions of CTAB-only provided a sufficient growth rate in the case of L-GSH-guided overgrowth from triangular Au plates as the CTAB/CTAC system led to achiral dendritic overgrowth (Fig. S4, ESI†). Returning to the nanocrystals produced by L-GSH-guided overgrowth from tetrahedra, they appear to have a roughly cubic profile (edge length:  $134 \pm 6$  nm, Fig. 2b) but actually consists of two flattened ellipsoids with pointed ends that are stacked on top of each other and offset by  $90^\circ$ . These ellipsoid-like features become evident from tilting a single particle (Fig. 2c–f). Notably, at  $45^\circ$  tilt (Fig. 2f), curvature to the ellipsoid-like features become evident and are a hallmark of intrinsically chiral nanocrystals. A more extensive SEM tilt study of this sample is also shown in Fig. S5 (ESI†).

Transmission electron microscopy (TEM) images of a single nanocrystal and corresponding electron diffraction patterns are shown in Fig. 2g–j, giving the projections from the [100] and [110] directions, respectively. The electron diffraction patterns indicate that these nanocrystals are single-crystalline, with the insets in Fig. 2g and i suggesting orientations that account for these observations. Taken together, the crystallographic relationship between the initial tetrahedral seeds and final nanocrystals can be analyzed as shown in Fig. S6 (ESI†). The superposition suggests that formation of chiral gap features is





**Fig. 3** Tomographical reconstruction of an overgrown Au plate (a–c) viewed from opposite edges (a and c) and top (b). (d) Experimental and (e) simulated optical properties of chiral nanocrystals from triangular plates. Tomographical reconstruction of an overgrown Au tetrahedron (f–h) viewed from [100], [111], and [110] directions, respectively. (i) Experimental and (j) simulated optical properties of chiral nanocrystals seeded by tetrahedra.

face-directed, consistent with literature.<sup>1,19</sup> Notably, when the same overgrowth procedure is conducted without L-GSH, nanocrystals without these gap features are produced as shown in Fig. S7 (ESI<sup>†</sup>). This observation indicates again that the chiral additive is required to achieve concave gap features.

Tomographical reconstructions of individual nanocrystals were obtained to further understand the 3D morphologies and verify their nanoscale chirality (see Fig. 3 and Videos S1 and S2 for the overgrown plates and tetrahedra, respectively, ESI<sup>†</sup>). Reconstructions of an overgrown plate and tetrahedron are shown at different orientations in Fig. 3a–c and f–h, respectively. The 2- and 3-fold rotational axes of the triangular Au plates are preserved in the overgrown product. The presence (or absence) of mirror symmetry, however, cannot be determined conclusively and is likely due to the intensity thresholding being unable to capture the subtle chiral gaps formed in the protrusions from the center of the nanoplates. Likewise, the 3- and 2-fold rotational axes of the tetrahedral seeds are preserved in the overgrown product. Generation of clockwise-handed features in the tetrahedral overgrowth is shown and compared to the 432 helicoid III system in Fig. S8 (ESI<sup>†</sup>), indicative of elimination of mirror symmetry.

Circular dichroism (CD) spectroscopy is well-suited to reveal chiroptical behavior by measuring the difference in absorbance of right- and left-circularly polarized light. The product nanocrystals have red-shifted localized surface plasmon resonances (LSPRs) compared to their seeds, consistent with their larger sizes (Fig. S9, ESI<sup>†</sup>).<sup>20–22</sup> While the seeds are not chiroptically active (Fig. S10, ESI<sup>†</sup>), both product nanocrystals show chiroptical behavior by CD spectroscopy (Fig. 3d and i). The *g*-factor response – which is normalized by extinction (see eqn (1)) – is lower in intensity for nanocrystals originating from the triangular Au plates compared to the overgrown tetrahedral system.

This difference likely stems from the mechanism of chiral feature generation, which has been proposed to occur at kink sites at the intersections of {100}, {110}, and {111} facets.<sup>1</sup> The triangular Au plates with  $D_{3h}$  symmetry express {111} basal facets and either {100} or {110} facets at the edges due to stacking faults, leading to a system with few of the hypothesized intersections that would favor chiral molecule adsorption. In contrast, the single-crystalline tetrahedral Au seeds are bound by {111} facets and rounded corners and edges, providing the hypothesized intersections that would facilitate expression of intrinsically chiral kink sites and generation of chiral features upon overgrowth.

Thus, the reconstructed nanocrystals were used as structural models in finite difference time domain (FDTD) simulations to verify the relationship between structure and chiroptical response.<sup>23</sup> A background index of 1.333 with circularly polarized light was used. As nanocrystals are randomly oriented in solution, the model orientation was rotated in the *x*- and *y*-directions (from 0°–180° in steps of 15°) relative to the injection axis of light (*z*-direction), consistent with previous methodology.<sup>1</sup> Fig. 3e and j shows the resulting averaged spectra of scattering and *g*-factor versus wavelength for the overgrown plates and tetrahedra, respectively. The complete simulated scattering spectra for all rotations are presented in Fig. S11 and S12 (ESI<sup>†</sup>) for the overgrown plates and tetrahedra, respectively. The experimental and simulated scattering spectra for both samples are in reasonably good agreement, showing a similar number of features reflective of the nanocrystals' symmetries.<sup>24</sup> Small spectral shifts and broadening for the experimental samples are evident and consistent with there being slight variations in structure from one nanocrystal to the next in a given sample.<sup>20,25</sup> CD signals are observed from simulations of the tomographically obtained models, indicating that the experimental-observed CD signals are not due to near-field enhancements of chiral molecules and rather the intrinsically chiral features of the nanocrystal. The negative *g*-factor feature present around 520 nm in Fig. 3i is likely due to byproducts in solution rather than an absorbance of the nanocrystals. This claim is further supported when comparing the simulated scattering and total extinction *g*-factor spectra (Fig. S13, ESI<sup>†</sup>), neither of which exhibit this negative response. Again, there is good agreement between experimental and simulated spectra, with slight variations likely due to the atomically imprecise nature of nanocrystals and the mesh size used in the simulations.

The larger *g*-factor achieved with the overgrown tetrahedral sample motivated further study into how its structure could be modified synthetically to achieve a larger response. Toward this effort, the concentrations of HAuCl<sub>4</sub> and L-GSH were systematically varied while keeping the total reaction volume and seed concentration constant, as the concentrations of overgrowth metal and chiral additive have been shown to influence chiral gap formation.<sup>19</sup> Increasing [HAuCl<sub>4</sub>] led to larger particles with modest increases in *g*-factor (column 3) that levels off or declines with further increasing [HAuCl<sub>4</sub>] (column 4). Increasing [L-GSH] leads to an increase in *g*-factor regardless of [HAuCl<sub>4</sub>]. At the highest [L-GSH], randomly segmented metal domains are evident in the nanocrystals (Fig. 4, row c, columns





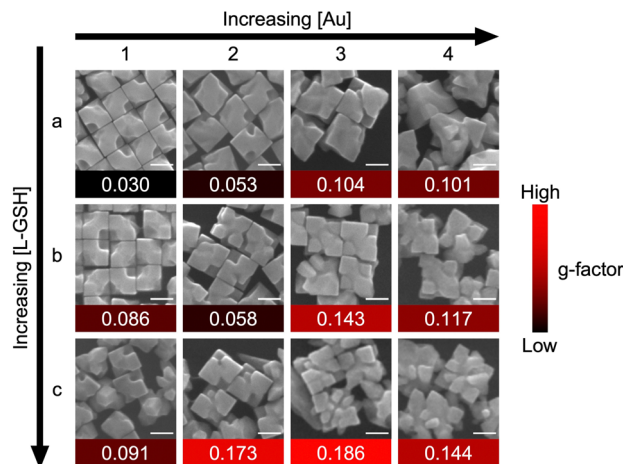


Fig. 4 SEM images from parameter sweep of L-GSH and Au precursor concentrations with measured  $g$ -factor. [L-GSH] is 4.6, 6.8, and 9.1  $\mu\text{M}$  in rows (a–c), respectively.  $[\text{HAuCl}_4]$  is 182.5, 365.0, 547.4, and 730.0  $\mu\text{M}$  in columns 1–4, respectively. Scale bars: 100 nm.

3 and 4), making structural determination challenging. The highest  $g$ -factor was associated with the sample in Fig. 4, row c, column 3 (see Fig. S14 for a SEM tilt study of single nanocrystal from this sample, ESI<sup>†</sup>), with the data suggesting that there is an optimal ratio of  $[\text{HAuCl}_4]$  to  $[\text{L-GSH}]$  to achieve nanocrystals with strong chiroptical response (*i.e.*, the diagonal) as is consistent with existing literature.<sup>19</sup> The variance in  $g$ -factor highlights the importance of optimizing the overgrowth conditions. Unfortunately, the exact structural origin of such changes in  $g$ -factor are unknown at this time given its high sensitivity to chiral gap dimensions, with systematic studies into the effects of chiral nanocrystal symmetry underway by simulation.

Taken together, intrinsically chiral nanocrystals with new symmetries are possible by selecting shape-controlled seeds of different symmetries, moving the community beyond the well-studied  $O_h$  case. While traditional seed-mediated syntheses typically result in symmetry transfer,<sup>26</sup> addition of chiral additives facilitates formation of chiroptically active nanocrystals. A prerequisite for chiral feature generation is the generation of transient kink sites that form at the junction of  $\{100\}$ ,  $\{110\}$ , and  $\{111\}$  faces. Notably, this work outlines a general colloidal pathway for chiral nanocrystals with different symmetries by pairing molecular templates with shape-controlled seeds.

S. E. S. and J. S. G. designed experiments. J. S. G. developed syntheses of chiral nanocrystals and conducted SEM, optoelectronic characterization and simulations. Z. J. W. acquired tilt SEM images. E. R. and G. R. L. acquired electron tomography data, which G. R. L. analysed with supervision of E. R. This manuscript was written through contributions of all authors and all approved the final version.

This work was supported by the US National Science Foundation Grant No. 1904499 and EU Framework Programme for Research and Innovation Horizon 2020 (ERC Starting Grant SPECS 804523). G. R. L. is thankful for funding from the EPSRC NanoDTC Cambridge (EP/L015978/1).

## Conflicts of interest

There are no conflicts to declare.

## Notes and references

- H.-E. Lee, H.-Y. Ahn, J. Mun, Y. Y. Lee, M. Kim, N. H. Cho, K. Chang, W. S. Kim, J. Rho and K. T. Nam, *Nature*, 2018, **556**, 360.
- J. García-Guirado, M. Svedendahl, J. Puigdollers and R. Quidant, *Nano Lett.*, 2018, **18**, 6279.
- J. Kumar, K. G. Thomas and L. M. Liz-Marzán, *Chem. Commun.*, 2016, **52**, 12555.
- S. D. Golze, S. Porcu, C. Zhu, E. Sutter, P. C. Ricci, E. C. Kinzel, R. A. Hughes and S. Neretina, *Nano Lett.*, 2021, **21**, 2919.
- J. Chen, X. Gao, Q. Zheng, J. Liu, D. Meng, H. Li, R. Cai, H. Fan, Y. Ji and X. Wu, *ACS Nano*, 2021, **15**, 15114.
- L. V. Besteiro, A. Movsesyan, O. Ávalos-Ovando, S. Lee, E. Cortés, M. A. Correa-Duarte, Z. M. Wang and A. O. Govorov, *Nano Lett.*, 2021, **21**, 10315.
- W. Xiao, K.-H. Ernst, K. Palotas, Y. Zhang, E. Bruyer, L. Peng, T. Greber, W. A. Hofer, L. T. Scott and R. Fasel, *Nat. Chem.*, 2016, **8**, 326.
- C. F. McFadden, P. S. Cremer and A. J. Gellman, *Langmuir*, 1996, **12**, 2483.
- S. W. Im, H.-Y. Ahn, R. M. Kim, N. H. Cho, H. Kim, Y.-C. Lim, H.-E. Lee and K. T. Nam, *Adv. Mater.*, 2020, **32**, 1905758.
- H.-E. Lee, R. M. Kim, H.-Y. Ahn, Y. Y. Lee, G. H. Byun, S. W. Im, J. Mun, J. Rho and K. T. Nam, *Nat. Commun.*, 2020, **11**, 263.
- M. L. Tseng, Z.-H. Lin, H. Y. Kuo, T.-T. Huang, Y.-T. Huang, T. L. Chung, C. H. Chu, J.-S. Huang and D. P. Tsai, *Adv. Opt. Mater.*, 2019, **7**, 1900617.
- A. Kuzyk, R. Schreiber, Z. Fan, G. Pardatscher, E.-M. Roller, A. Högele, F. C. Simmel, A. O. Govorov and T. Liedl, *Nature*, 2012, **483**, 311.
- R. G. Weiner, M. R. Kunz and S. E. Skrabalak, *Acc. Chem. Res.*, 2015, **48**, 2688.
- L. Chen, F. Ji, Y. Xu, L. He, Y. Mi, F. Bao, B. Sun, X. Zhang and Q. Zhang, *Nano Lett.*, 2014, **14**, 7201.
- V. Germain, J. Li, D. Ingert, Z. L. Wang and M. P. Pileni, *J. Phys. Chem. B*, 2003, **107**, 8717.
- Y. Zheng, W. Liu, T. Lv, M. Luo, H. Hu, P. Lu, S.-I. Choi, C. Zhang, J. Tao, Y. Zhu, Z.-Y. Li and Y. Xia, *Chem. – Asian J.*, 2014, **9**, 2635.
- M. M. Bower, C. J. DeSantis and S. E. Skrabalak, *J. Phys. Chem. C*, 2014, **118**, 18762.
- N. Ortiz and S. E. Skrabalak, *Langmuir*, 2014, **30**, 6649–6659.
- N. H. Cho, G. H. Byun, Y.-C. Lim, S. W. Im, H. Kim, H.-E. Lee, H.-Y. Ahn and K. T. Nam, *ACS Nano*, 2020, **14**, 3595.
- E. Ringe, J. M. McMahon, K. Sohn, C. Cobley, Y. Xia, J. Huang, G. C. Schatz, L. D. Marks and R. P. Van Duyne, *J. Phys. Chem. C*, 2010, **114**, 12511.
- S. Link and M. A. El-Sayed, *J. Phys. Chem. B*, 1999, **103**, 4212.
- P. K. Jain, K. S. Lee, I. H. El-Sayed and M. A. El-Sayed, *J. Phys. Chem. B*, 2006, **110**, 7238.
- A. O. Govorov, *J. Phys. Chem. C*, 2011, **115**, 7914.
- J. D. Smith, Z. J. Woessner and S. E. Skrabalak, *J. Phys. Chem. C*, 2019, **123**, 18113.
- A. F. Smith, R. G. Weiner, M. M. Bower, B. Dragnea and S. E. Skrabalak, *J. Phys. Chem. C*, 2015, **119**, 22114.
- S. E. Skrabalak, *Acc. Mater. Res.*, 2021, **2**, 621.

